Journal of Inorganic Biochemistry 283 (2026) 113369

Contents lists available at ScienceDirect

Journal of Inorganic Biochemistry

journal homepage: www.elsevier.com/locate/jinorgbio

Suppression of glioblastoma progression by novel Phthalocyanine derivatives: In vitro characterization and molecular docking analysis

Şuranur Ayvaz [a], Nevzat Batan [a], Cihan İnan [a], Halil İbrahim Güler [a], İsmail Değirmencioğlu [b,*]

[a] Karadeniz Technical University, Faculty of Science, Department of Molecular Biology and Genetics, 61080 Trabzon, Türkiye
[b] Karadeniz Technical University, Faculty of Science, Department of Chemistry, 61080 Trabzon, Türkiye

ARTICLE INFO

Keywords:
Glioblastoma
Phthalocyanine
Subphthalocyanine
Morpholine
Docking
Cytotoxicity

ABSTRACT

Glioblastoma multiforme (GBM) is the most common and aggressive primary brain tumor in adults. Despite standard treatment prognosis remains poor due high recurrence and rapid therapeutic resistance, highlighting the need for new agents targeting alternative pathways. Phthalocyanines represent chemically versatile scaffolds with favorable photophysical and structural properties; however, present study focused specifically on their dark-condition in vitro biological effects rather than photodynamic activity. In this study, two novel water-soluble silicon (IV) phthalocyanine and boron subphthalocyanine derivatives were synthesized for the first time via cyclotetramerization, and water-soluble derivatives were obtained by quaternization with methyl iodide (CH_3I) in chloroform at room temperature in dark. The antiproliferative and scratch assay-based migration-modulating effects of these compounds were assessed in U-87 MG glioblastoma cells under dark conditions. MTT assays showed time- and dose-dependent decreases in viability, with 72 h IC_{50} values of 15.46 μM (SiPc (**4**)) and 25.52 μM (SubPc (**5**)). Colony formation assays indicated marked suppression of clonogenic capacity, and scratch assays demonstrated significant inhibition of migration. To gain mechanistic insight, molecular docking was performed against focal adhesion kinase (FAK) and DNA topoisomerase IIα (TOP2A); both compounds showed favorable predicted binding to the active sites, with SiPc (**4**) displaying a stronger interaction profile. Redocking of co-crystallized ligands yielded RMSD values below 2.0 Å, supporting protocol reliability. Overall, these findings suggest preliminary dark-condition in vitro activity of SiPc (Tan et al., 2020 (4)) and SubPc (Weller et al., 2021 (5)) against U-87 MG cells, while the docking results offer hypothesis-generating molecular insight into possible target interactions that may support future mechanistic and optimization studies.

1. Introduction

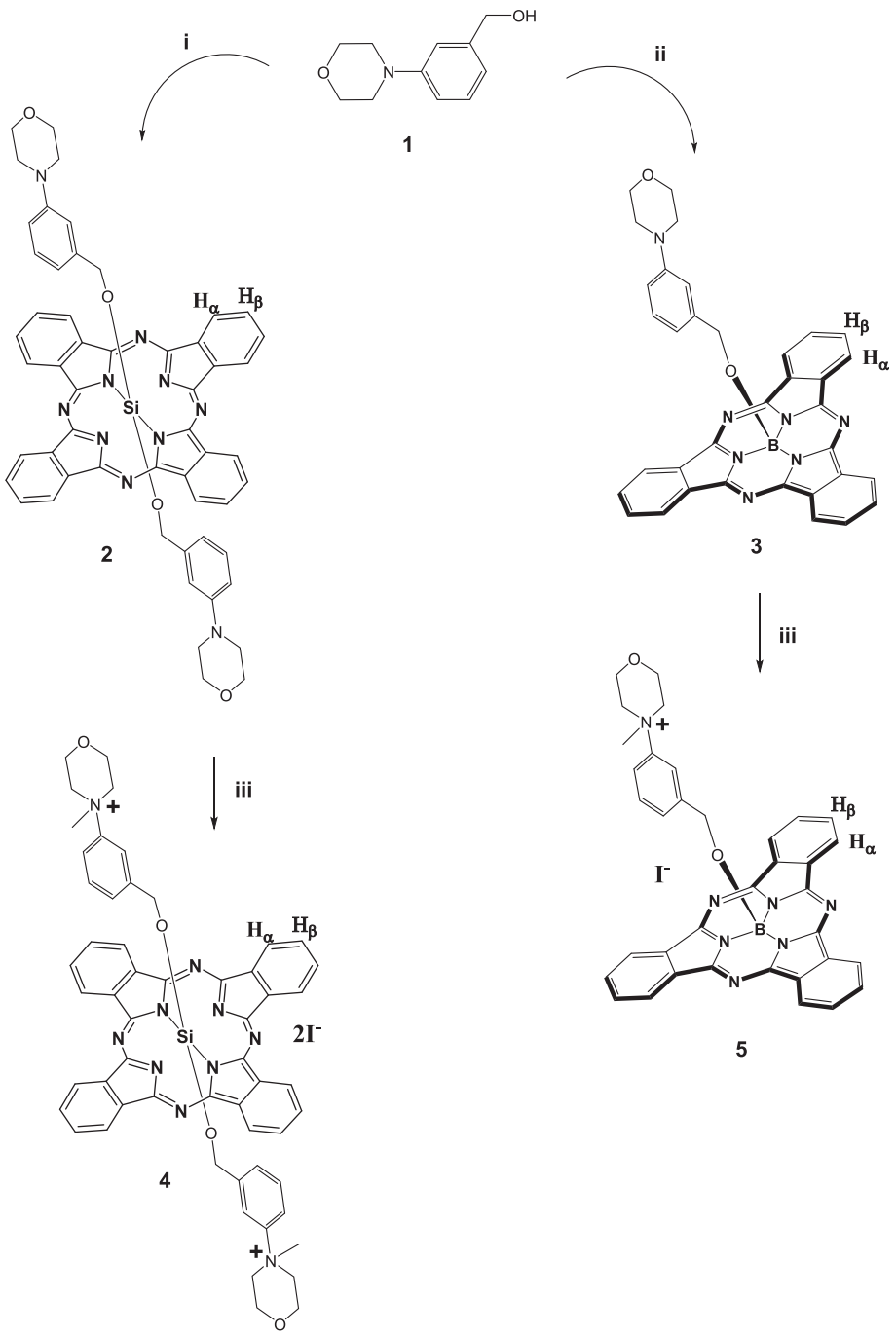
Glioblastoma, the most common and aggressive brain tumor marker, manifests as uncontrolled growth of glial cells. This hysterical structure accounts for approximately 30% of brain tumors and about 80% of malignant intracranial neoplasms [1]. Due to the severity of the disease, only 5.6% of glioma patients survive for five years or more after diagnosis before succumbing to the illness [2,3]. Despite significant advancements in standard treatments such as surgery, chemotherapy, and radiotherapy, along with emerging cancer therapies, the life expectancy and quality of life for these patients still fall short of desired levels [4,5]. The blood-brain barrier comprises three main components: cerebral capillary endothelium, astrocytes, and pericytes. This remarkable structure serves as a critical interface between the central nervous system and endothelial cells [6]. In glioblastoma patients, a malfunctioning blood-brain barrier prevents the removal of toxins, pathogens, and other harmful waste products from the body. This also limits the absorption of essential therapeutic drugs [7].

The primary factors that impede the delivery of therapeutic and diagnostic agents to their target sites are the extracellular environments that obstruct access to the body, such as the skin and mucous membranes, as well as blood components and associated structures. Ensuring

Abbreviations: GBM, Glioblastoma multiforme; FAK, focal adhesion kinase;; TOP2A, DNA topoisomerase IIα; PEG, polyethylene glycol; Pc, phthalocyanine; SubPcCl, boron subphthalocyanine chloride; DMEM, Dulbecco's Modified Eagle Medium; FBS, fetal bovine serum; PSA, penicillin – streptomycin - amphotericin B; MTT, 3-(4,5-dimethylthiazol-2-yl)-2,5-diphenyltetrazolium bromide; DMSO, dimethyl sulfoxide; LGA, Lamarckian Genetic Algorithm; RMSD, root-mean-square deviation; EGFR, epidermal growth factor receptor.

* Corresponding author.
E-mail address: ismail61@ktu.edu.tr (İ. Değirmencioğlu).

https://doi.org/10.1016/j.jinorgbio.2026.113369
Received 10 February 2026; Received in revised form 23 May 2026; Accepted 31 May 2026
Available online 1 June 2026
0162-0134/© 2026 Elsevier Inc. All rights are reserved, including those for text and data mining, AI training, and similar technologies.



Scheme 1. The reaction pathway of morpholineoxy-substituted Pcs (**2–5**). i. $SiPcCl_2$ - NaH / dry toluene – 36 h, ii. SubPcCl - NaH / dry toluene – 24 h, iii. CH_3I – chloroform / room temperature - 96 h.

compatibility and optimizing these key factors allows drugs to better adapt to their environment, ultimately leading to effective healing. Drugs in the bloodstream, particularly those that are hydrophilic, may occasionally struggle to reach their intended targets on the surface of cells. In these instances, they might exhibit deficiencies in the endosomal or lysosomal regions, which are crucial pathways for their uptake into cells [8,9]. When the target region is a subcellular organelle such as a mitochondrion or the nucleus, cationically charged materials appear to be more effective on the target region. This mechanism involves electrostatic interactions between the positive charge of cationic phthalocyanine (Pc) and the negative charge of the target organelle, such as mitochondria, making the process leading to apoptosis more appealing. Furthermore, the lipophilicity of the molecule, the P0/w partition coefficient, and the aliphatic/aromatic characteristics of the substituted groups also play crucial roles in cell death. Experimental data show that cationic sensitizers initially disrupt the inner mitochondrial membrane system of cancerous cells, causing this membrane structure to eventually break down into amorphous and crystalline vesicles. This process leads to the desired cell death [10–13].

Phthalocyanines are a class of aromatic heterocyclic compounds that play a crucial role in various applications, including liquid crystals, electrochemical devices, gas sensors, solar cells, biological imaging modules, semiconductors, and catalysis [14–17]. Due to the water-averse nature of these remarkable molecules, their application is limited in crucial areas like cancer treatment. However, significant modifications to their peripheral positions can enhance their solubility.

Particularly, the excellent solubility of molecules with quaternary nitrogen, carboxylic groups, polyethylene glycol (PEG) chains, and sulfonyl groups in aqueous environments has made them valuable in biological studies. The addition of metallic or non-metallic elements like Zn, Si, and B to the phthalocyanine ring enhanced the physicochemical properties and biological activity of the resulting molecule [18–20].

Silicon is the second most abundant element in nature after carbon, making it essential in various vital materials. The advancement of modern biotechnological methods has enabled the production of biohybrid materials that can be applied in a wide range of fields. Currently, delicate biomolecules, functional proteins, enzymatic structures, and living cellular units can be effectively protected by biomineral silica frameworks. This favorable situation enables the precise delivery of either a single drug or a combination of drugs. Additionally, improved knowledge regarding the use of biogenic silicon materials suggests that future scientific teams working with these materials will achieve more successful outcomes [21–24]. Significant improvements in the treatment of prostate [25], cervical [26], colorectal [27], lung cancer, and sarcoma [28] have been achieved thanks to a boron-based material. This advancement results from boron's extensive effects on various types of cancer. Therefore, the dynamic potential of boron stands out, providing hope in the battle against sarcomas.

Currently, there are only a few studies examining the cancer-fighting properties of phthalocyanines when supplemented with morpholine. These studies mainly focus on the cytotoxic effects of various metal-centered phthalocyanine compounds, including zinc, cobalt, copper, manganese, and silicon, on different types of cancer cells. Furthermore, the activities of these molecules in inhibiting enzymes were also assessed [12,29–31]. In this study, we evaluated the dark-condition antiproliferative and antimetastatic effects, as well as their cell viability, wound healing, and colony-forming capabilities of synthesized substituted morpholine-ringed phthalocyanine molecules on glioblastoma cells for the first time.

2. Experimental

2.1. Material and methods

(3-morpholinophenyl)methanol (**1**), $SiPcCl_2$ and SubPc were purchased from Sigma Aldrich. UV–Vis spectra were recorded by Perkin Elmer Lambda 25 spectrometer, using 1 cm path length cuvettes at room temperature. The reaction pathway was depicted in Scheme 1. FT-IR, NMR, mass spectra were recorded by Perkin Elmer One, Agilent 400 MHz NMR spectrometer and Maldi MS Microflex. MTT absorbance was measured at 570 nm using a microplate reader (Multiskan Sky, Thermo Scientific). Colony formation and wound healing assays were visualized under an inverted microscope (Axiovert 5, Zeiss). All chemicals used in biochemical studies were purchased from Sigma Aldrich. The spectral data were given as supplementary materials.

2.2. Synthesis of the compounds

2.2.1. Diaxially morpholineoxy-substituted silicon Pc (2)

Dry toluene (10 mL), silicon phthalocyanine dichloride ($SiPcCl_2$) (0.07 g, 0.16 mmol) and compound (**1**) (0.06 g, 0.32 mmol) were added to the two-necked reaction flask. NaH (0.01 g, 0.32 mmol) was added to it, which was stirred in an argon atmosphere at room temperature and the temperature was increased to 110 °C. After 36 h, the reaction was terminated and crude product was purified by column chromatography (silica gel 60, $CHCl_3$ - acetone (10,1, *v*/v) as eluent). Yield: 74.21% (0.21 g). Melting point >300 °C.

FT-IR (ATR) υ_{max} /cm^{-1}: 3054 (Ar-CH), 2961–2918 (Aliph. -CH), 1600, 1519, 1427, 1333, 1289 (pH-C-O), 1120 (C—N), 1077, 910, 758, 727.

^{1}H NMR (400 MHz, 25 °C, $CDCl_3$): δ(ppm) 9.62–9.60 (m, 8H / Pc-H_α), 8.37–8.35 (bs, 8H / Pc-H_β), 6.97 (s, 2H / Ar—H), 6.90–6.87 (m, 6H / Ar—H), 3.90–3.88 (m, 8H / -CH_2), 3.21–3.19 (m, 8H / -CH_2), (−0.74) (s, 4H / -$SiOCH_2$).

Uv-vis (DMSO, 1 × 10^{-5} M): λ_{max} /nm (log ε): 672 (4.99), 643 (4.09), 605 (4.16), 355 (4.49).

MALDI MS (*m/z*): Calculated: 925.097; Found: 925.058 $[M]^+$ for $C_{54}H_{44}N_{10}O_4Si$.

2.2.2. Axially morpholineoxy-substituted SubPc (3)

Dry toluene (10 mL), boron subphthalocyanine chloride (SubPcCl) (0.1 g, 0.23 mmol) and compound (**1**) (0.16 g, 0.81 mmol) were added to the two-necked reaction flask. NaH (0.02 g, 0.81 mmol) was added to it, which was stirred in an argon atmosphere at room temperature and the temperature was increased to 110 °C. After 24 h, the reaction was terminated and crude product was purified by column chromatography (silica gel 60, $CHCl_3$ - acetone (20:1, *v*/v) as eluent). Yield: 35% (0.11 g).

FT-IR (ATR) υ_{max} /cm^{-1}: 3058 (Ar-CH), 2951–2850 (Aliph. -CH), 1711, 1678, 1611, 1453, 1377, 1326, 1296 (Ph-C-O), 1115 (C—N), 1077, 995, 738, 719.

^{1}H NMR (400 MHz, 25 °C, $CDCl_3$): δ(ppm) 8.87–8.85 (m, 6H / Pc-H_α), 7.93–7.91(m, 6H / Pc- H_β), 6.89–6.85 (t, *J* = 7.9 Hz, 1H / Ar—H), 6.49–6.47 (dd, *J* = 8.2, 2.3 Hz, 1H / Ar—H), 5.99–5.97 (d, *J* = 7.5 Hz, 1H / Ar—H), 5.87 (s, 1H / Ar—H), 3.78–3.76 (m, 4H / -CH_2), 2.90–2.88 (m, 4H / -CH_2), 2.62 (s, 2H / -$BOCH_2$).

Uv-vis (DMSO, 1 × 10^{-5} M): λ_{max} /nm (log ε): 562 (4.78), 510 (4.23), 303 (4.53).

MALDI MS (*m/z*): Calculated: 587.450; Found: 587.345 $[M]^+$ for $C_{35}H_{26}BN_7O_2$.

2.2.3. General procedure for synthesis of water-soluble silicon and subphthalocyanines

In a single-necked flask, morpholineoxy subs. SiPc (**2**) (0.14 g, 0.15 mmol) and subs. SubPc (**3**) (0.1 g, 0.23 mmol) were dissolved with chloroform (3 mL). They were stirred with iodomethane (3.5 mL) at room temperature in the dark for 96 h. Water-soluble phthalocyanines (**4** and **5**) was filtered off, washed with $CHCl_3$.

2.2.4. Diaxially water-soluble silicon phthalocyanine (4)

Yield: 46.89% (0.14 g). Melting point >300 °C.

FT-IR (ATR) υ_{max} /cm^{-1}: 3054 (Ar-CH), 2958–2917 (Aliph. -CH), 1609, 1518, 1427, 1332, 1289 (Ph-C-O), 1117 (C—N), 1067, 909, 758, 728.

^{1}H NMR (400 MHz, 25 °C, DMSO-d_6): δ(ppm) 9.70–9.67 (m, 8H / Pc-H_α), 8.56–8.54 (m, 8H / Pc-H_β), 7.84 (m, 2H / Ar—H), 7.80–7.78 (dd, *J* = 8.3, 2.6 Hz, 2H / Ar—H), 7.66–7.62 (t, *J* = 8.0 Hz, 2H / Ar—H), 7.57–7.55 (d, *J* = 7.5 Hz, 2H / Ar—H), 4.37–4.34 (m, 8H / -CH_2), 3.72–3.67 (m, 8H / -CH_2), 3.51 (s, 6H / -CH_3), (−0.71) (s, 4H / -$SiOCH_2$).

Uv-vis (DMSO, 1 × 10^{-5} M): λ_{max} /nm (log ε): 675 (4.87), 609 (4.09), 358 (4.47).

MALDI MS (*m/z*): Calculated:1208.976; Found: 1083.829 $[M - I + H]^+$, 955.605 $[M - 2I]^+$ for $C_{56}H_{50}I_2N_{10}O_4Si$.

2.2.5. Axially water-soluble subphthalocyanine (5)

Yield: 89.68% (0.11 g).

FT-IR (ATR) υ_{max} /cm^{-1}: 3056 (Ar-CH), 2956–2849 (Aliph. -CH), 1719, 1688, 1601, 1454, 1377, 1286 (Ph-C-O), 1112 (C—N), 1087, 995, 738, 718.

^{1}H NMR (400 MHz, 25 °C, $CDCl_3$): δ(ppm) 8.87–8.85 (m, 6H / Pc-H_α), 7.93–7.91(m, 6H / Pc- H_β), 6.89–6.85 (t, *J* = 7.8 Hz, 1H / Ar—H), 6.49–6.47 (dd, *J* = 8.2, 2.3 Hz, 1H / Ar—H), 5.99–5.97 (d, *J* = 7.5 Hz, 1H / Ar—H), 5.87 (s, 1H / Ar—H), 3.78–3.76 (m, 4H / -CH_2), 3.27–3.24 (m, 3H / -CH_3), 2.90–2.88 (m, 4H / -CH_2), 2.62 (s, 2H / -$BOCH_2$).

Uv-vis (DMSO, 1 × 10^{-5} M): λ_{max} /nm (log ε): 563 (4.99), 512 (4.49), 303 (4.80).

MALDI MS (*m/z*): Calculated: 729.390; Found: 602.001 $[M-I]^+$ for $C_{36}H_{29}BIN_7O_2$.

2.3. Cell culture and reagents

Human glioblastoma cell line U-87 MG (HTB-14) was maintained in Dulbecco's Modified Eagle Medium (DMEM, Gibco) supplemented with 10% fetal bovine serum (FBS, Capricorn Scientific), 1% penicillin – streptomycin - amphotericin B (1% PSA, Invitrogen, Gibco, UK). Cells were incubated in a humidified atmosphere with 5% CO_2 at 37 °C.

2.4. Cell viability assay

Cell viability was determined using the 3-(4,5-dimethylthiazol-2-yl)-2,5-diphenyltetrazolium bromide (MTT) colorimetric assay (GoldBio). In 96-well plates, U-87 MG cells were seeded with a density of 1×10^4 cells/well. After 24 h of incubation, cells were treated with SiPc (4) and SubPc (5) at concentrations of 0.05, 0.1, 1, 5, 10, 15, 20 and 25 μM for 24, 48, and 72 h. To evaluate the potential effects of the vehicle, cells were additionally treated with 0.005, 0.01, 0.1, 0.5, 1, 1.5, 2, and 2.5% dimethyl sulfoxide (DMSO) for 72 h. Following treatment, the MTT assay was performed according to the manufacturer's instructions, and absorbance was measured at 570 nm using a microplate reader. Cell viability was calculated by normalizing absorbance values to those of non-treated control cells, which were defined as 100%. IC_{50} values were obtained from normalized viability data using nonlinear regression with a variable-slope dose–response model in GraphPad Prism version 8.2.1. The analyses were performed using data from at least three independent biological experiments, and the corrected IC_{50} values are provided in Table S2. During treatments with the corrected concentration range, no visible precipitation was observed, and the final DMSO concentration in compound-treated wells was kept at or below 0.1% (*v*/v).

2.5. Colony formation assay

The colony formation assay was performed to evaluate the reproductive viability of U-87 MG cells as described previously [32]. Briefly, cells were seeded in 6-well plates at a density of 1000 cells/well. After 24 h, following cell attachment, the culture medium was replaced with medium containing 15.46 μM SiPc (4) or 25.52 μM SubPc (5). After 72 h of treatment, the medium was replaced with fresh, untreated medium, and cells were further incubated for 12 days to allow colony formation. Then, colonies were fixed with 100% methanol for 20 min at + 4 °C and stained with 0.1% crystal violet for 5 min at room temperature. The stained colonies in each well were visualized using an inverted microscope and analyzed by counting colony numbers and measuring colony diameters. The assay was performed in three independent biological replicates. Colony number and diameter were quantified from representative microscopic images using calibrated image analysis software, and the data were expressed as mean ± standard deviation relative to the untreated control group.

2.6. Scratch assay

U-87 MG cells were seeded into 6-well plate at a density of 2×10^5 cell/well and cultured until approximately 90% confluency. A linear scratch was then generated using a sterile 10 μL pipette tip. After washing with 1× PBS to remove the floating cells, U-87 MG cells were incubated in medium containing 15.46 μM SiPc (4) and 25.52 μM SubPc (5) for 24, 48 and 72 h. Cell migration was observed at 0, 24, 48 and 72 h time points, 4 random pictures under inverted microscope were taken for each wound. Wound gap widths were measured using the calibrated distance measurement tool in ZEISS ZEN 3.12 software. The region of interest was defined as the cell-free area between the two wound edges, and wound closure was determined by comparing the gap width at 24, 48, and 72 h with the initial gap width at 0 h. The wound closure percentage was calculated using the formula: wound closure (%) = [(gap width at 0 h − gap width at the indicated time point) / gap width at 0 h] × 100. For normalized comparison, the control group at each time point was set to 100%, and treated groups were expressed relative to the corresponding control [33].

2.7. Molecular docking study

To provide preliminary structure-based insight into possible molecular interactions that may be related to the observed inhibition of cell migration and colony formation in U-87 MG glioblastoma cells, molecular docking studies were conducted against focal adhesion kinase (FAK) and DNA topoisomerase IIα (TOP2A), which are involved in cancer cell motility, invasion, survival signaling, and DNA replication during tumor progression [34–37].

The crystal structures of the human FAK kinase domain co-crystallized with a small-molecule inhibitor (PDB ID: 4I4E, Res: 1.55 Å) and the human TOP2A–DNA complex bound to etoposide (PDB ID: 5GWK, Res: 3.15 Å) were retrieved from the Protein Data Bank. Protein preparation was carried out using UCSF ChimeraX [38] and BIOVIA Discovery Studio Visualizer (BIOVIA, 2019). Missing residues and side chains were inspected and completed where necessary using the structure-editing tools implemented in ChimeraX. Subsequently, the protein structures were processed using the Dock Prep module in ChimeraX, which included the removal of crystallographic water molecules and non-essential heteroatoms, addition of polar hydrogen atoms, assignment of appropriate protonation states corresponding to physiological pH, and application of Kollman united-atom charges. Co-crystallized ligands were retained during this process for redocking-based validation. The prepared protein structures were finally converted into AutoDock-compatible PDBQT format for docking calculations.

The silicon- and boron-containing compounds evaluated in the in vitro assays were prepared for docking using Avogadro version 1.2.0 [39]. Initial three-dimensional ligand geometries were optimized using the MMFF94 force field to relieve steric strain and obtain energetically reasonable conformations. Special care was taken to preserve correct valence states and formal charges, particularly for boron and silicon atoms, which possess non-classical coordination environments. Following geometry optimization, ligand torsions were defined, Gasteiger partial charges were assigned, and ligands were converted into PDBQT format using AutoDockTools. Multiple rotatable bonds were allowed to ensure adequate conformational sampling during docking.

Molecular docking calculations were performed using AutoDock 4.2 [40]. The docking grids were defined based on the coordinates of the co-crystallized ligands to ensure accurate representation of the active binding sites. For FAK (PDB: 4I4E), the grid box was centered on the ATP-binding pocket with dimensions of 60 × 60 × 60 grid points and a grid spacing of 0.375 Å, sufficiently covering the hinge region and surrounding catalytic residues. For TOP2A (PDB: 5GWK), the grid box encompassed the etoposide binding site at the protein–DNA interface using identical grid spacing (0.375 Å) and dimensions optimized to fully include the DNA–protein interaction region critical for enzyme inhibition.

Docking simulations were carried out using the Lamarckian Genetic Algorithm (LGA). For each ligand–protein pair, 100 independent docking runs were performed with a population size of 150 individuals, a maximum of 2.5×10^6 energy evaluations, and default AutoDock genetic algorithm parameters. The resulting docked conformations were clustered using a root-mean-square deviation (RMSD) tolerance of 2.0 Å.

To validate the docking protocol, redocking studies were conducted by re-docking the native ligands (FAK inhibitor in 4I4E and etoposide in 5GWK) into their respective binding sites. The docking methodology was considered reliable when the lowest-energy docked pose reproduced the experimentally observed binding mode with an RMSD value below 2.0 Å (typically <1.5 Å), a widely accepted criterion for docking accuracy [40,41].

The best-ranked docking poses were selected based on binding energy scores and cluster population. Protein–ligand interactions,

including hydrogen bonds, π–π stacking, hydrophobic contacts, and electrostatic interactions, were analyzed and visualized using BIOVIA Discovery Studio Visualizer (BIOVIA, 2019). Comparative interaction analyses were performed to assess differences in binding modes between the two compounds and to correlate docking results with the observed in vitro inhibition of migration and clonogenic survival in U-87 MG cells.

2.8. Statistical analysis

Data were analyzed using GraphPad Prism version 8.2.1 (San Diego, USA) and are presented as means ± standard deviation (SD) and all experiments were conducted with at least three independent replicates. Statistical significance was determined by student *t*-test, one-way or two-way ANOVA followed by a post-hoc Tukey test when necessary. *P* values were set as $p < 0.05$ (*), $p < 0.01$ (**), $p < 0.001$ (***) and $p < 0.0001$ (****).

3. Results and discussion

3.1. Synthesis and characterization

The preparation process for morpholineoxy-substituted Pcs (**2** and **3**) and their quaternized fragments (**4** and **5**) is summarized in Scheme 1. The morpholineoxy-substituted silicon Pc (**2**) was synthesized by reacting the starting compound (**1**) with $SiPcCl_2$. Similarly, the morpholineoxy-substituted SubPc (**3**) was produced by reacting the starting compound (**1**) with SubPcCl. The water-soluble Pcs (**4** and **5**) were obtained by mixing compounds **2** and **3** in $CHCl_3$ in the presence of CH_3I.

The FTIR spectrum of the substituted silicon Pc (**2**) shows characteristic vibrations that support the formation of the molecule. These include aromatic and aliphatic C—H stretching vibrations at 3054 cm^{-1} and within the range of 2961–2918 cm^{-1}. Additionally, C=C stretching vibrations are observed between 1600 and 1427 cm^{-1}, (Ph-C-O) vibrations at 1289 cm^{-1}, and (C—N) vibrations at 1120 cm^{-1}. A similar situation occurred with minor shifts in the FTIR spectrum of substituted SubPc (**3**). All of this data supported the merging based on FTIR analysis [12,29,31].

In the ^1H NMR spectrum of substituted SiPc (**2**) (Fig. S1), the unsubstituted aromatic protons (H_α and H_β) of the compound resonated in the higher ppm region, with values between 9.62 and 9.60 and 8.37–8.35 ppm. In contrast, the morpholinoxy protons located in the axial positions resonated within the range of 6.97–6.87 ppm. The aliphatic protons that comprise the remainder of the molecule appear as a multiplet in the range of 3.90 to 3.19 ppm. The magnetic anisotropy generated by the silicon-centered cavity has caused the CH_2 protons coordinated to silicon to shift to the basic region at a value of −0.74 ppm. Similarly, the unsubstituted aromatic protons of SubPc (**3**) (Fig. S3) appeared as two distinct multiplets within the ranges of 8.87–8.85 ppm and 7.93–7.91 ppm. Aromatic morpholine protons in the axial position resonated between 6.89 and 5.87 ppm. The CH_2 protons in the morpholine ring appeared as multiplets at 3.78–3.76 ppm and 2.90–2.88 ppm. The non-ring CH_2 protons coordinating from the oxygen to the boron center shifted further upfield, appearing as singlets at 2.62 ppm [12,29–31,42,43].

Quaternized forms of SiPc (**2**) and SubPc (**3**) molecules were obtained by precipitating them in the medium after mixing with a large amount of CH_3I at room temperature and in the dark. The FTIR spectra of molecules (**4**) and (**5**) showed minimal differences due to the addition of methyl groups; only shifts in existing peaks were observed.

The unsubstituted protons of the quaternized SiPc (**4**) (Fig. S5) resonate in a downfield, compared to compound (**3**). Similarly, the protons of the morpholine ring also appear in the downfield. The CH_3 protons, coordinated with the nitrogen part of the molecule, appeared as singlets at 3.51 ppm. The remaining protons (CH_2) were detected in their expected regions. The same situation occurred in the quaternized SubPc (**5**) (Fig. S7) molecule. In this structure, the relevant protons maintained their positions with minimal shifts compared to their previous state. Moreover, the methyl protons in the structure appeared as a multiplet in the upfield region, with values of 3.27–3.24 ppm [12,29–33]. The molecular ion peaks of all Pcs were measured at the expected value, 925.058 $[M]^+$ scale for subs. SiPc (**2**) (Fig. S2), 587.345 $[M]^+$ scale for subs. SubPc (**3**) (Fig. S4), 1083.829 $[M - I + H]^+$ scale for water-soluble SiPc (**4**) (Fig. S6), and 602.001 $[M\text{-}I]^+$ scale for water-soluble SubPc (**5**) (Fig. S8) respectively.

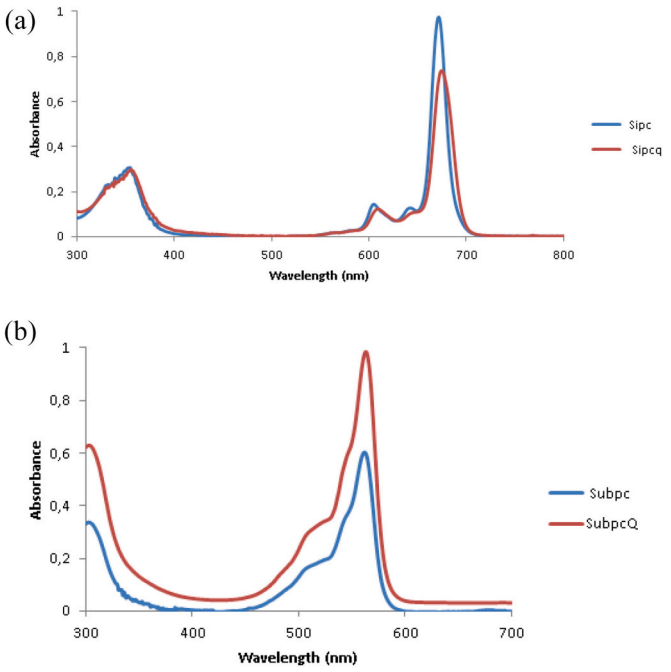


Fig. 1. a. UV–vis absorption spectra of subs. SiPc (**2**) and SiPcq (**4**) in DMSO. b. UV–vis absorption spectra of subs. SubPc (**3**) and SubPcq (**5**) in DMSO.

Pc molecules create a moderately strong B band in the blue area. They also create a strong Q band in the red area. This makes them useful in many fields. Metal-free phthalocyanines have different molecular symmetry. They form two strong, equal peaks in the NIR region. These peaks relate to $\pi \rightarrow \pi^*$ transitions. Metal-containing components form absorbance with different peak intensities. This is due to greater degeneracy. In this study, the UV–vis spectra of all studied phthalocyanines (**2–5**) were recorded in DMSO at 1×10^{-5} M concentration. The Q bands of the studied phthalocyanines were observed at 672, 643 and 605 nm for SiPc (**2**), 562 and 510 nm for SubPc (**3**), 675 and 609 nm for the methyl adducted SiPc (**4**), and 563 and 512 nm for the methyl adducted SubPc (**5**) (see experimental section) (Fig. 1). The B bands were observed at 356 nm for (**2**), 303 nm for (**3**), 358 nm for (**4**), and 303 nm for (**5**), respectively (Fig. 1-b). Additionally, UV–Vis spectral graphs were generated for 0.1% dilutions of the molecules prepared by dilution with the culture medium (Fig. S9 and S10). All these values are compatible with the D_{4h} symmetry of metallo phthalocyanines and C_3 symmetry of SubPc [12,29–31,42–45].

3.2. SiPc (4) and SubPc (5) inhibit cell proliferation of the U-87 MG cell line

Cell viability of U-87 MG cells treated with SiPc (**4**) and SubPc (**5**) for 24, 48, and 72 h was evaluated using the MTT test. Our results showed that treatment of U-87 MG cells with 0.05, 0.1, 1, 5, 10, 15, 20 and 25 μM SiPc (**4**) and SubPc (**5**) for 24, 48 and 72 h significantly reduced cell viability in a dose- and time-dependent manner (Table S1). At 72 h, U-87 MG cells treated with 0.05, 0.1, 1, 5, 10, 15, 20 and 25 μM SiPc (**4**) showed a significant decrease of cell viability to 98.27 ± 9.60, 91.90 ±

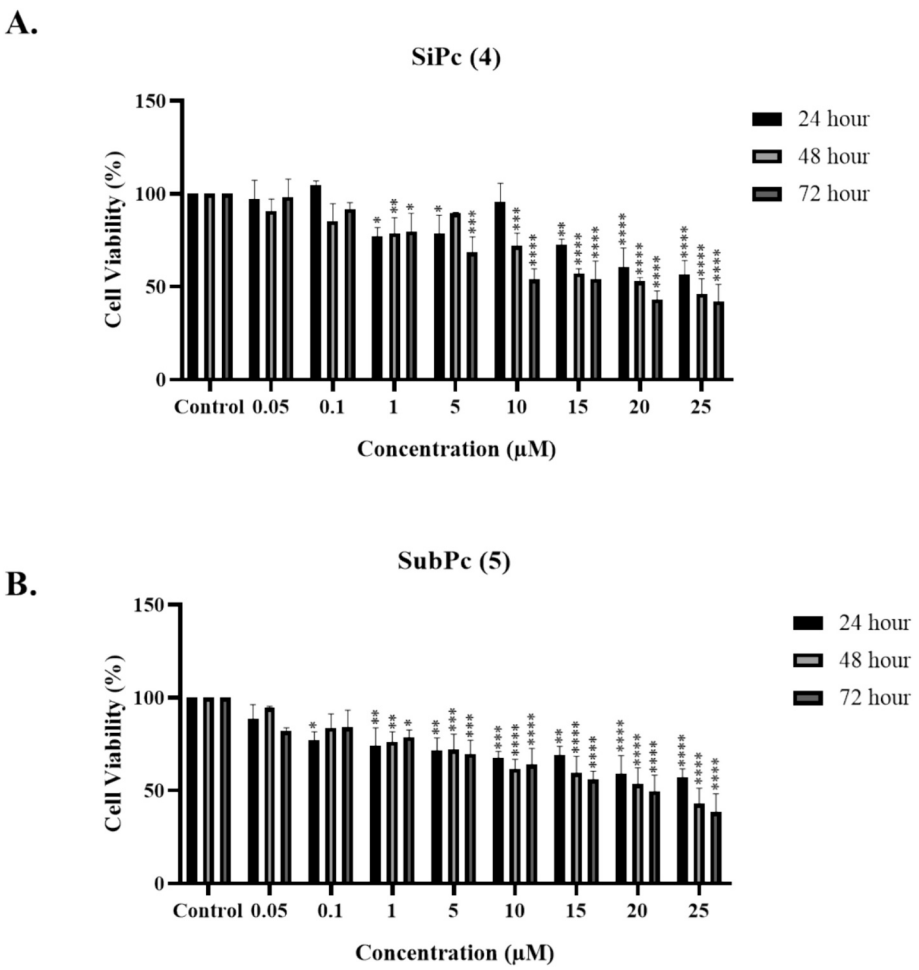


Fig. 2. Percentage of cell viability determined after treatment of U-87 MG cells with 0.05, 0.1, 1, 5, 10, 15, 20, 25 μM (A) SiPc (**4**) and (B) SubPc (**5**) for 24, 48 and 72 h. Data are presented as mean ± standard deviation (SD) values of three independent experiments. Statistical significance was evaluated relative to the control group (*$p < 0.05$; **$p < 0.01$; ***$p < 0.001$; ****$p < 0.0001$).

3.46, 79.95 ± 9.64, 68.60 ± 8.15, 54.06 ± 5.58, 54.35 ± 9.49, 43.13 ± 4.66 and 42.32 ± 9.04, respectively (Fig. 2A). Under the same experimental conditions, treatment with SubPc (**5**) resulted in a significant decrease of cell viability to 82.23 ± 1.58, 84.03 ± 9.27, 78.66 ± 3.98, 69.81 ± 7.20, 64.11 ± 8.61, 55.97 ± 4.44, 49.87 ± 8.43, and 38.43 ± 9.91 at the corresponding concentrations (Fig. 2B). IC_{50} values were calculated for U-87 MG cell lines treated with SiPc (**4**) and SubPc (**5**) for 24, 48, and 72 h (Table S2). After 72 h, the IC_{50} values of U-87 MG cells treated with SiPc (**4**) and SubPc (**5**) were calculated as 15.46 μM and 25.52 μM, respectively. Based on the observed time-dependent cytotoxic effects, the 72 h time point was selected for subsequent experiments. Both compounds reduced cell viability at increasing doses, exhibiting a dose-dependent cytotoxicity profile. The morpholine ring acts as a pharmacophore in many small molecule targeted agents, and these agents can exhibit potent cytotoxic effects in various cancer types. For instance, Gefitinib, an epidermal growth factor receptor (EGFR) tyrosine kinase inhibitor, is a quinazoline derivative containing a morpholine group and exhibits cytotoxicity in EGFR-mutant cancer cells. A recent study reported that synthesized morpholine-substituted quinazoline derivatives also possessed significant antiproliferative effects in breast (MCF-7), lung (A549), and neuroblastoma (SH-SY5Y) cell lines [46]. These findings suggest that the morpholine ring, when added to the drug in the appropriate molecular context, can enhance pharmacological efficacy and cell permeability. Similarly, the fact that the compounds in our study significantly reduced cell viability confirms that these molecules are cytotoxic to GBM cells. Therefore, although novel compounds containing a morpholine ring are effective at high concentrations on their own, these early results suggest that they may have stronger antitumor potential with further structure-activity relationship investigations and possible derivative optimizations in future studies.

The synthesized compounds were dissolved in dimethyl sulfoxide (DMSO). To exclude the possibility that the observed cytotoxic effects were attributable to the solvent, the impact of DMSO alone on cell viability was evaluated. The cell viability values obtained after 72 h of treatment of the U87 cell line with 0.005, 0.01, 0.1, 0.5, 1, 1.5, 2, and 2.5% DMSO were calculated as 98.02 ± 7.31, 86.75 ± 7.63, 85.26 ± 3.55, 71.46 ± 2.52, 67.11 ± 2.79, 66.01 ± 1.99, 66.54 ± 3.80, and 45.13 ± 5.58, respectively, and the IC_{50} value was calculated as 4.59 (Fig. S11). Stock solutions of the synthesized compounds were prepared in DMSO. To exclude any potential solvent-related effects on cell viability and to ensure that the observed biological responses were attributable solely to the test compounds, the impact of DMSO alone was systematically evaluated. When the effects of DMSO concentrations up to 2.5% on U-87 MG cell viability were evaluated during 72 h of treatment, it was observed that DMSO concentrations of 0.1% and below had no effect on cell viability. In contrast, DMSO at 1% and above showed a significant cytotoxic effect, and at approximately 4–5% DMSO levels, it led to the death of half of the cells (IC_{50} 4.59). These findings indicate that DMSO is generally tolerable at low percentages, but can become toxic to cells above the threshold of 0.5–1%. Consistent with these results, previous studies have reported that DMSO is generally considered safe at concentrations between 0.1% and 0.5% (*v*/v), whereas levels

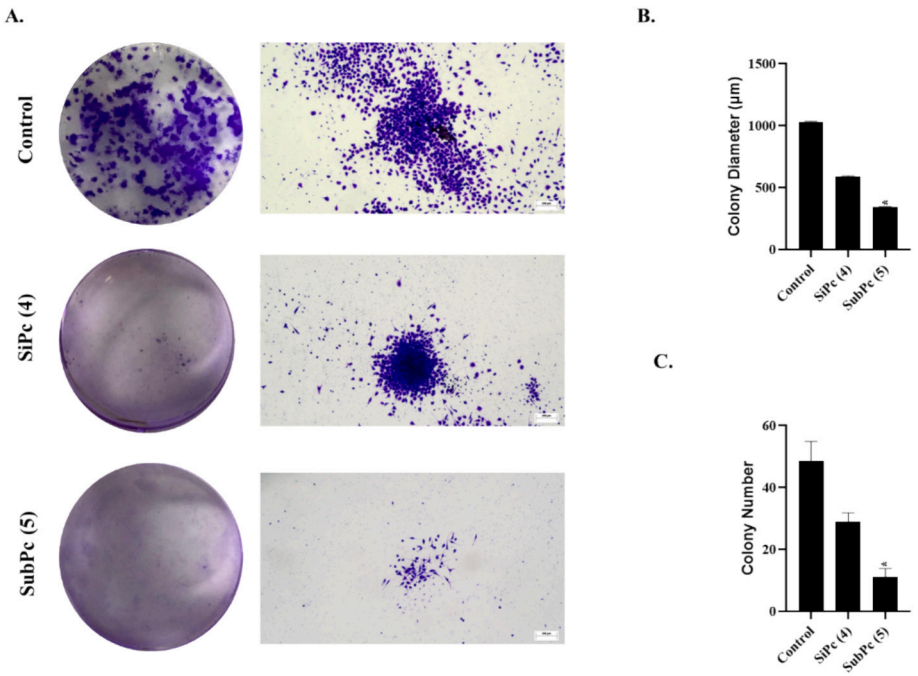


Fig. 3. Effects of treatment with 15.46 µM SiPc (**4**) and 25.52 µM SubPc (**5**) on the colony formation potential of U-87 MG cells after 12 days. (A) Representative macroscopic images of colonies formed in the wells (left panel) and microscopic images of U-87 MG cell colonies obtained using a 5× objective (right panel). Scale bars represent 200 µm. (B) Comparison of colony diameters among control, SiPc (**4**), and SubPc (**5**) treatment groups. (C) Quantitative analysis of colony numbers in control, SiPc (**4**), and SubPc (**5**) groups. Data are presented as the mean ± standard deviation (SD) of three independent experiments (*$p < 0.05$).

exceeding 0.6% may impair cell proliferation in certain cancer cell lines [47]. Therefore, the fact that the volume of DMSO used as a solvent in our experiments was kept at 0.1% or less emphasizes that the observed effects of the compounds were not DMSO-related. DMSO control experiments showed that the applied DMSO level was within the safe limit for the cells and that the cytotoxicity and anti-migration effects were entirely due to the biological activity of the compounds, not the solvent. Thus, the potential interference effect of DMSO was excluded in the interpretation of the experimental results, and the true biological effects of the compounds were revealed.

3.3. Morpholine-derived compounds reduce the colony-forming potential of U-87 MG cells

The colony formation assay was performed to assess the long-term reproductive capacity of single cells. The effects of SiPc (**4**) and SubPc (**5**) on the colony-forming ability of U-87 MG cells were evaluated. The findings revealed that the average colony diameter in the control group was 1030.81 ± 3.77 µm. Treatment with SiPc (4) reduced the average colony diameter to 587.75 ± 8.13 µm, whereas SubPc (5) significantly decreased it to 342.22 ± 4.81 µm (Fig. 3B). Similarly, the total number of colonies was 48.50 ± 6.36 in the control group. SiPc (4) reduced the colony number to 29.00 ± 2.83, while SubPc (5) caused a statistically significant decrease to 11.00 ± 2.84 (Fig. 3C). These results indicate that SubPc (5) significantly reduced both colony size and colony number in U-87 MG cells (*$p < 0.05$), whereas SiPc (4) showed a decreasing trend under the same experimental conditions. Reduced colony formation is considered a significant indicator of anti-proliferative effect. In the present study, the colony formation assay showed that SubPc (5) significantly reduced the long-term colony-forming capacity of U-87 MG cells. Although SiPc (4) also decreased colony number and colony diameter compared with the control group, this reduction did not reach statistical significance under the tested conditions (Fig. 3). These findings suggest that SubPc (5) exerted a more pronounced inhibitory effect on clonogenic growth than SiPc (4). SubPc (**5**) caused a greater decrease in colony diameter and number compared to SiPc (**4**). Similar clonogenic inhibitory effects have been reported for various anticancer agents. For instance, anethol, a naturally occurring component, significantly reduced colony number and inhibited clonal growth in U87-MG cells even at low micromolar concentrations [48]. Likewise, Fan et al. (2018) reported that the gastrointestinal motility drug trimebutine significantly decreased both cell survival and colony-forming ability in glioma cell lines in a dose-dependent manner [49]. Additionally, it has been reported that morpholine-based two copper(II) compounds inhibit colony formation in A549 cells [49]. Our findings clearly demonstrate that novel morpholine-based compounds prevent long-term proliferation in GBM cells, and are consistent with the clonogenic effects of anticancer agents in the literature. The suppression of colony formation by SiPc (**4**) and SubPc (**5**) indicates that these compounds not only induce acute cytotoxicity but also restrict the long-term proliferation and colony-forming ability of the cells. This is a significant finding suggesting that these novel molecules may reduce the potential for tumor recurrence and progression in GBM treatment. Specifically, the reduction in colony formation suggests that these compounds may inhibit clonal proliferation by targeting clonal subgroups within the GBM cell population.

3.4. Morpholine-derived compounds decrease migration ability of U-87 MG cell line

The in vitro migration ability of the U-87 MG cell line was evaluated using a scratch assay at 24, 48 and 72 h after treatment with 15.46 µM SiPc (**4**) and 25.52 µM SubPc (**5**) (Fig. 4). According to the findings, compared to the control group, wound closure occurred in the group treated with SiPc (**4**) at 24, 48, and 72 h at rates of 77.61 ± 0.06%, 77.28 ± 8.65%, and 80.37 ± 5.02%, respectively. Similarly, wound closure rates in cells treated with SubPc (**5**) were measured as 21.49 ± 9.23%, 25.81 ± 6.51%, and 31.47 ± 5.21%, respectively (Fig. 4B). These data reveal that both compounds significantly suppress cell migration. One of the major clinical challenges of GBM is that tumor cells can spread microscopically within brain tissue, leading to recurrence even after surgical resection [48]. Therefore, agents that inhibit tumor cell

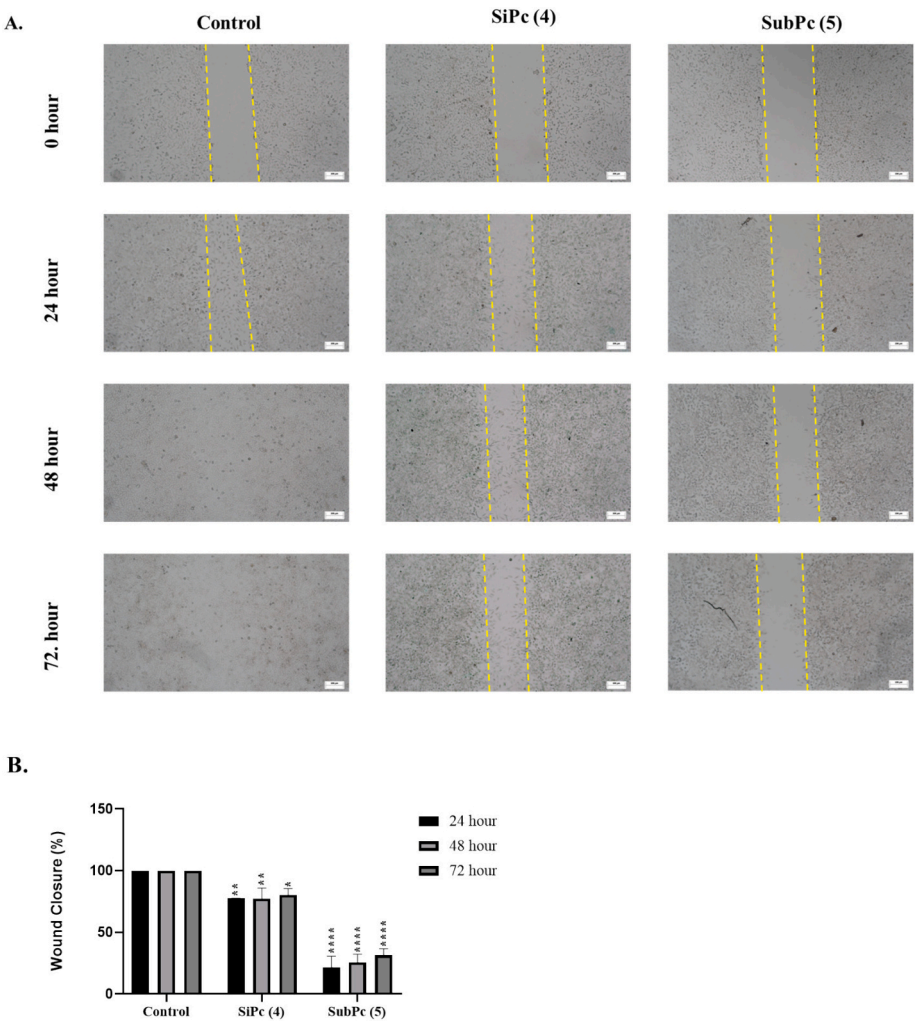


Fig. 4. Effects of treatment with 15.46 μM SiPc (**4**) and 25.52 μM SubPc (**5**) on wound closure (cell migration) potential of U-87 MG cells at 24, 48, and 72 h. (A) Following growth to confluence, a scratch was created in the cell monolayer, and wound closure was monitored by microscopic imaging at 0, 24, 48, and 72 h. Scale bars represent 200 μm. (B) Quantitative analysis of wound closure percentages in cells treated with SiPc (**4**) and SubPc (**5**) compared to the control group. Data are presented as the mean ± standard deviation (SD) of three independent experiments (*$p < 0.05$; **$p < 0.01$; ****$p < 0.0001$).

migration and invasion are critically important in the treatment of GBM. In the present study, scratch assay analyses demonstrated that both morpholine-derived compounds significantly suppressed the migratory capacity of U-87 MG cells compared with the control group, with SubPc (**5**) exhibiting a more pronounced inhibitory effect. This was evidenced by a marked reduction in wound closure rates over time. The dose-dependent reduction in cell migration reveals the anti-metastatic and anti-invasive potential of the compounds in vitro conditions. There is increasing evidence in the literature that various compounds can inhibit GBM cell migration. A previous study showed that a newly synthesized morpholine-based compound reduced the wound closure rate in MDA-MB-231 cells [50]. In another study, piperlongumin was shown to strongly inhibit cell migration in a dose-dependent manner in U87 MG and LN229 glioblastoma cells using a scratch model [51]. In anticancer compounds containing morpholine scaffolds, the morpholine group facilitates the entry of the compound into the cell and its accumulation in specific organelles. This reduces not only the cytotoxic effect but also processes such as cell migration and invasion. In studies of morpholin-functionalized photosensitizers, determining where the effect occurs is crucial due to the short half-life and limited diffusion distance of the reactive species formed. Therefore, directing the effect to a specific region, such as the lysosome, can enhance treatment and, depending on the concentration, may also contribute to the suppression of migration/invasion [52]. In our study, similar to the literature, in control cells, the wound largely closed within 24–48 h, while in cells treated with both morpholine compounds, the rate of wound closure was significantly slowed. Even after 72 h, wounds remained largely open in the treatment groups, and cell migration was reported to be considerably reduced compared to the control group.

3.5. *Molecular docking*

To generate preliminary structure-based hypotheses that may help guide future mechanistic studies, molecular docking analyses were performed for SiPc (**4**) and SubPc (**5**) against focal adhesion kinase (FAK; PDB ID: 4I4E) and DNA topoisomerase IIα (TOP2A; PDB ID: 5GWK). These two enzymes were selected based on their well-established roles in regulating tumor cell motility, survival signaling, DNA replication, and long-term proliferative capacity in glioblastoma and other aggressive cancers [34,35]. FAK was selected because of its involvement in focal adhesion turnover, cytoskeletal remodeling, and migration-associated signaling, whereas TOP2A was selected due to its role in DNA topology regulation and proliferation-related DNA processing. However, the docking analysis was intended only as an exploratory computational approach and was not designed to confirm direct target engagement or enzymatic inhibition.

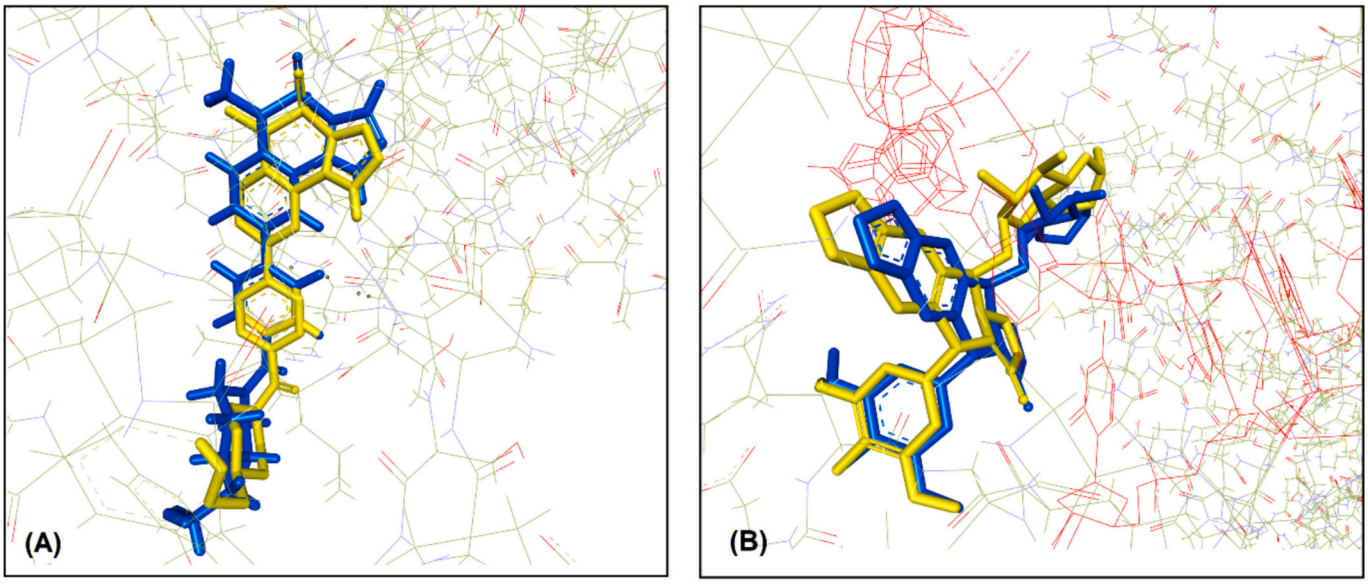


Fig. 5. Redocking validation of the docking protocol for FAK and TOP2A. (A) Superposition of the co-crystallized and redocked ligands in FAK (PDB ID: 4I4E). (B) Superposition of the co-crystallized etoposide and redocked pose in TOP2A (PDB ID: 5GWK). Redocked poses reproduced the native binding modes with RMSD values below 2.0 Å.

Table 1
Molecular docking-derived binding energies and key interactions of SiPc (**4**) and SubPc (**5**) targeting FAK and TOP2A.

Receptor	Ligand	Predicted Binding Energy (kcal/mol)	Estimated K_i value***	Number of H-bonds	Number of Residues within 4 Å	Interacting Key Residues
Focal Adhesion Kinase (4I4E)	SiPc (**4**)	−10.69	14.65 nM	4	11	Ile428, Arg426, Ala452, Met499, Leu501, Cys502, Gly505, Glu506, Leu553
	SubPc (**5**)	−9.20	179.02 nM	2	11	Ile428, Val436, Leu501, Glu506
	*reference	−8.71	409.89 nM	4	9	Arg426, Ile428, Val436, Ala452, Val484, Met499, Cys502, Leu504, Leu553
DNA Topoisomerase IIα (5GWK)	SiPc (**4**)	−12.68	510.44 pM	4	13	Met327, Met331, DC8, DC11, DA12
	SubPc (**5**)	−9.62	88.56 nM	6	7	Arg52, Met327, Met331, DC8, DA12, DG13
	** reference	−8.26	877.50 nM	6	5	Asp28, Gly27, Arg52, Met331, DC8, DG13

* [4-(2-hydroxyethyl)piperidin-1-yl][4-(5-methyl-4,4-dioxido-1,5-dihydropyrazolo[4,3-c][2,1]benzothiazin-8-yl)phenyl]methanone.
** (5S,5aR,8aR,9R)-9-(4-hydroxy-3,5-dimethoxyphenyl)-8-oxo-5,5a,6,8,8a,9-hexahydrofuro[3′,4′,6,7]naphtho[2,3-d][1,3]dioxol −5-yl 4,6-O-[(1*R*)-ethylidene]-beta-D-glucopyranoside.
*** K_i values were calculated by AutoDock 4.2 based on estimated binding free energies.

Prior to docking of the test compounds, the reliability of the docking protocol was validated by redocking the native co-crystallized ligands into their respective binding sites. The redocked poses of the FAK inhibitor in 4I4E and etoposide in 5GWK reproduced the experimentally observed binding conformations with root-mean-square deviation (RMSD) values below 2.0 Å, supporting the technical reliability of the docking protocol for reproducing the crystallographic binding poses (Fig. 5).

Docking analysis against FAK revealed that SiPc (**4**) exhibits a markedly stronger predicted binding affinity toward the ATP-binding pocket compared to SubPc (**5**) and the reference ligand. SiPc (**4**) showed a predicted binding energy of −10.69 kcal/mol with an estimated K_i value of 14.65 nM, whereas SubPc (**5**) displayed a weaker affinity (−9.20 kcal/mol; K_i = 179.02 nM). The co-crystallized reference inhibitor showed the lowest affinity among the tested ligands (−8.71 kcal/mol; K_i = 409.89 nM) (Table 1). Structurally, SiPc (**4**) was predicted to be deeply accommodated within the catalytic cleft of FAK, occupying the hinge and adjacent hydrophobic regions in a manner comparable to, yet more extensive than, the native ligand (Fig. 6A). At the molecular level, SiPc (**4**) formed multiple predicted stabilizing interactions with key residues lining the ATP-binding pocket. Two π–lone pair interactions were observed with Ile428 at distances of approximately 2.75 Å and 2.84 Å, anchoring the aromatic core of the ligand within the hinge region. In addition, carbon hydrogen bonds were established with Gly505 at distances of 1.69 Å and 2.43 Å, while a conventional hydrogen bond with Gly505 (2.84 Å) and an additional conventional hydrogen bond with Glu506 (2.65 Å) were detected (Table 1). These interactions were complemented by hydrophobic contacts involving Arg426, Ala452, Met499, Leu501, and Leu553, collectively suggesting a favorable predicted binding mode of SiPc (**4**). In contrast, SubPc (**5**) formed fewer hydrogen bonds and lacked the extensive hinge-region engagement observed for SiPc (**4**), consistent with its reduced predicted affinity (Fig. 7A).

FAK plays a central role in focal adhesion turnover and actin cytoskeleton remodeling, processes that directly govern cancer cell migration and invasion [35]. Therefore, the predicted interaction network of SiPc (**4**) within the FAK active site may provide a plausible structural hypothesis that could be explored in future FAK-focused validation studies, rather than direct evidence of FAK inhibition.

Docking against TOP2A further highlighted SiPc (**4**) as the most potent binder among the tested ligands. SiPc (**4**) demonstrated a predicted binding energy of −12.68 kcal/mol and an estimated K_i of 510.44 pM, substantially outperforming SubPc (**5**) (−9.62 kcal/mol; K_i = 88.56 nM) and the reference ligand (−8.26 kcal/mol; K_i = 877.50 nM)

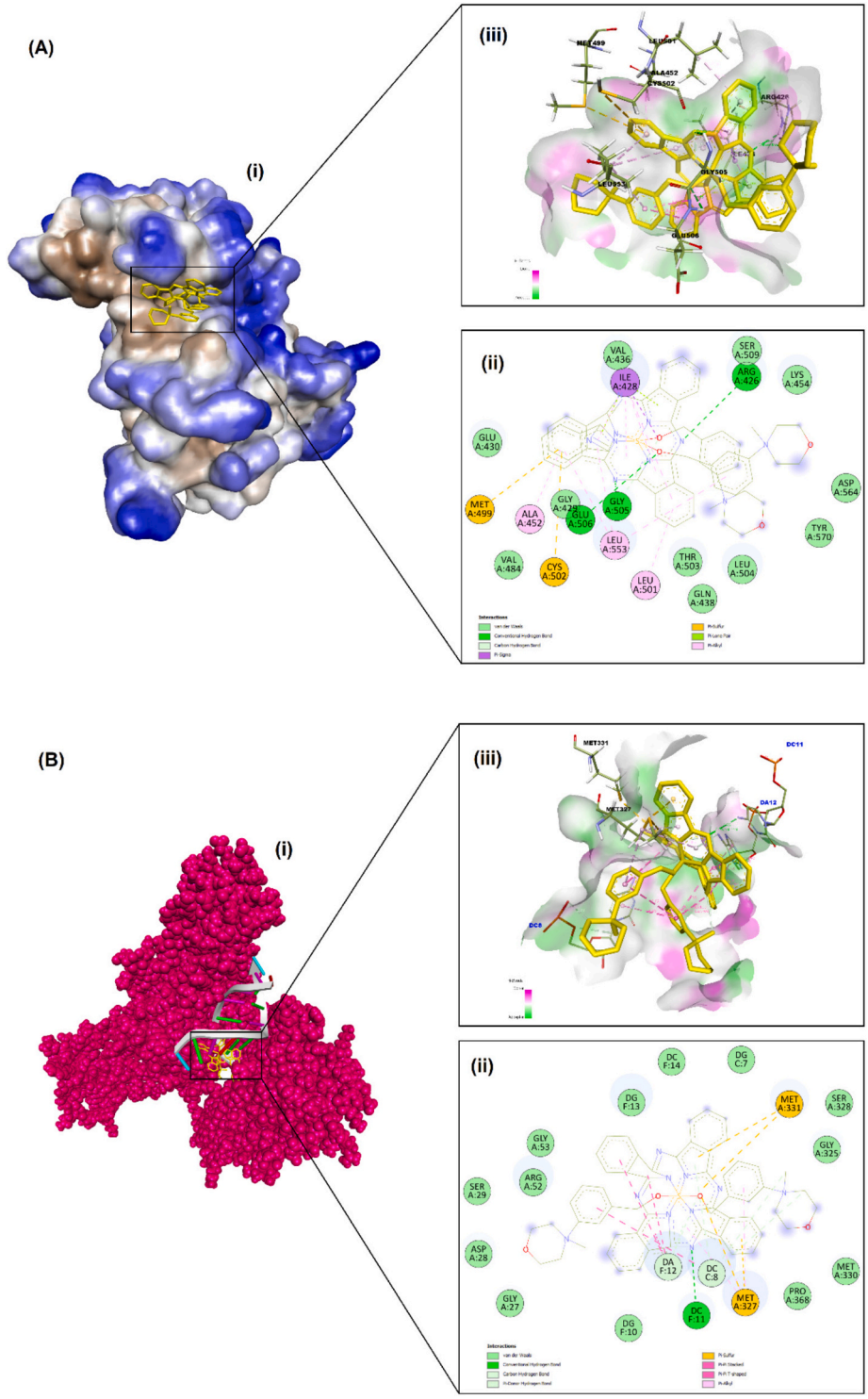


Fig. 6. Binding mode of SiPc (**4**) in focal adhesion kinase (A) and DNA topoisomerase IIα active sites (B). (i) Surface representation of the binding pockets showing the accommodation of SiPc (**4**). (ii) Two-dimensional interaction diagrams highlighting key protein–ligand interactions. (iii) Three-dimensional docking pose of SiPc (**4**) within the active sites.

(Table 1). The docking pose of SiPc (**4**) overlapped with the etoposide-binding region at the protein–DNA interface, suggesting a possible binding orientation compatible with the TOP2A–DNA cleavage complex region (Fig. 6B).

Detailed interaction analysis revealed that SiPc (**4**) was predicted to interact with both protein residues and DNA bases critical for TOP2A catalytic function. Multiple hydrogen bonds and carbon hydrogen bonds were detected, including interactions with DC11 (1.87 Å), DA12 (2.75 Å), and DC8 (carbon hydrogen bonds at 2.89 Å and 3.66 Å), as well as hydrophobic contacts with Met327 and Met331 (Table 1). Such interaction patterns are characteristic of effective TOP2A poisons, which stabilize the cleavage complex and disrupt DNA religation, ultimately impairing DNA replication and cell proliferation [34]. Although SubPc (**5**) formed a higher number of hydrogen bonds within the TOP2A complex, its weaker predicted binding energy and less optimal positioning suggest a reduced overall stabilization compared to SiPc (**4**)

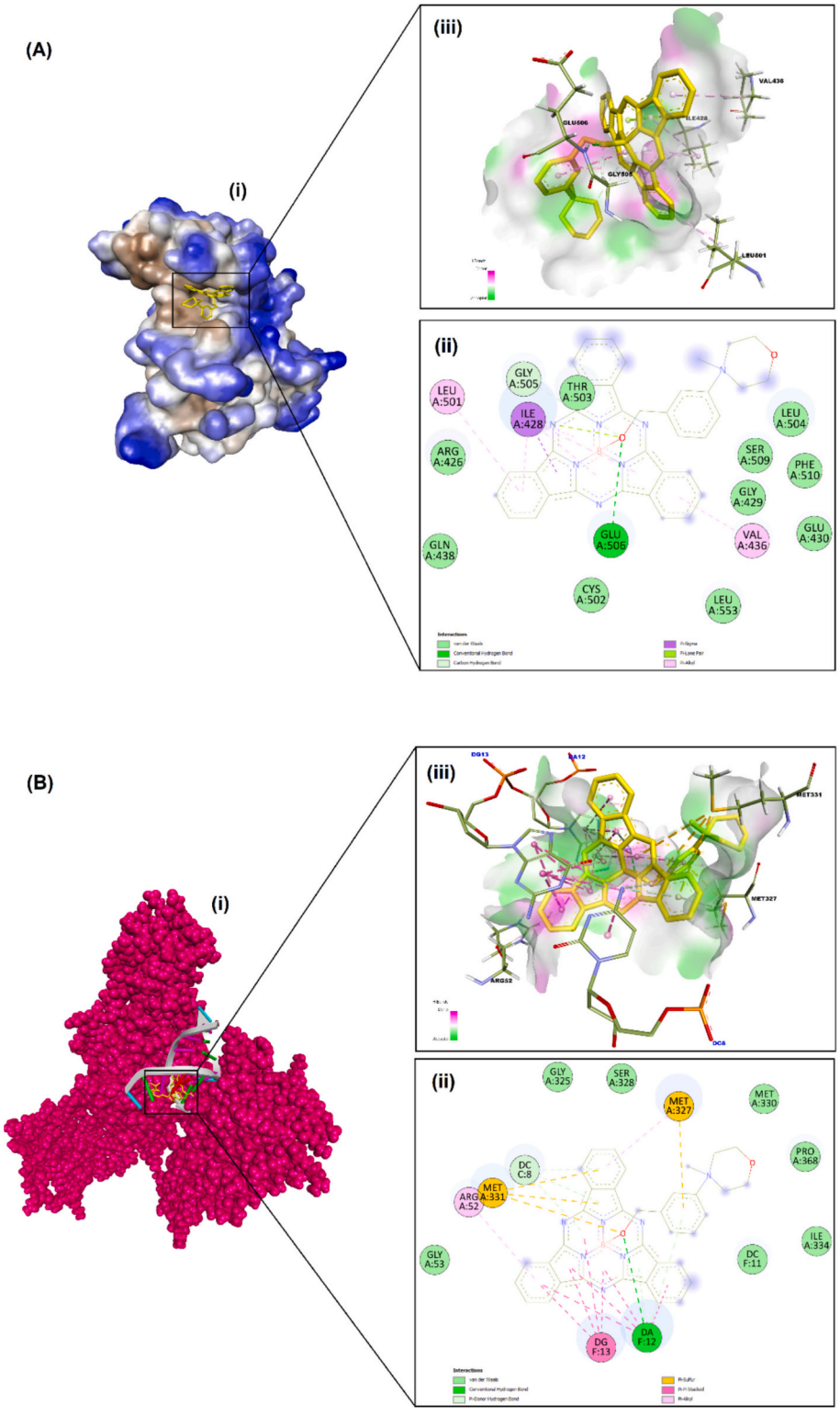


Fig. 7. Binding mode of SubPc (**5**) in focal adhesion kinase (A) and DNA topoisomerase IIα active sites (B). (i) Surface representation of the binding pockets showing the accommodation of SubPc (**5**). (ii) Two-dimensional interaction diagrams highlighting key protein–ligand interactions. (iii) Three-dimensional docking pose of SubPc (**5**) within the active sites.

(Fig. 7B).

When evaluated comparatively across both targets, SiPc (**4**) consistently exhibited stronger predicted binding affinities, lower estimated K_i values, and more favorable interaction networks than SubPc (**5**) and the reference ligands (Table 1). These computational findings are broadly consistent with the stronger in vitro activity of SiPc (4), but they do not establish a causal relationship between FAK/TOP2A binding and the observed cellular effects. Instead, the predicted FAK and TOP2A interactions should be considered preliminary hypotheses that may help guide future target-validation experiments. Similar correlations between docking-predicted affinities and biological activity have been reported for FAK and TOP2A inhibitors in previous structure-based

studies [34,35,41].

Overall, the integrated docking analysis suggests a potential dual-target mechanism of action for SiPc (**4**), linking its superior in vitro anti-glioblastoma activity to simultaneous interference with migration-associated signaling via FAK and proliferation-associated DNA processing via TOP2A.

4. Conclusion

Compounds containing morpholine rings offer several advantages in cancer drug development due to their favorable physicochemical properties and associated biological activities. Particularly in central nervous system tumors such as glioblastoma, the ability of a candidate molecule to cross the blood-brain barrier, achieve sufficient bioavailability, and demonstrate efficacy in the target tissue is critically important. Morpholine scaffolds, thanks to their suitable pharmacochemical properties, allow for the design of molecules that can meet these requirements; they also pave the way for the development of multiple mechanisms of action targeting key signaling pathways involved in GBM progression, such as PI3K/mTOR, FAK, or CXCR4 [53]. In this study, two novel morpholin derivative compounds showed time- and concentration-dependent antiproliferative activity and reduced scratch assay-based wound closure in U-87 MG glioblastoma cells. The compounds reduced cell viability in a dose-dependent manner, suppressed colony-forming potential, and decreased the scratch assay-based migratory response of U-87 MG cells. These findings are in line with the biological advantages of the morpholine pharmacophore reported in the literature and suggest that this chemical core may represent a useful chemical framework for further investigation in aggressive tumors such as glioblastoma. Although the presence of a morpholine ring alone does not ensure clinical efficacy, next-generation morpholine derivatives may overcome earlier limitations through improved selectivity, optimized pharmacological profiles, and reduced off-target toxicity. In this context, the strong in vitro effects of the compounds evaluated in our study and their inclusion of the morpholine structure offer a significant advantage in terms of investigating their efficacy in in vivo brain tumor models in the future. In conclusion, the present study provides a hypothesis-generating computational insight of the anti-glioblastoma activity of SiPc (**4**) and SubPc (**5**) by integrating in vitro findings with structure-based molecular docking analyses. The strong predicted binding of SiPc (**4**) to focal adhesion kinase and DNA topoisomerase IIα offers a structural rationale for its pronounced anti-migratory and anti-clonogenic effects observed in U-87 MG cells. Docking validation through redocking confirmed the reliability of the computational protocol, strengthening the credibility of the proposed interactions. Overall, these results support the dual-target potential of SiPc (**4**) and highlight its promise as a lead candidate for further optimization and advanced preclinical evaluation. These new morpholine-derived compounds stand out as innovative and versatile therapeutic candidates targeting uncontrolled cell proliferation and invasion in the treatment of glioblastoma. Considering the flexibility and multi-targeting capacity offered by morpholine chemistry, it is predicted that advances in this field will contribute to the development of more effective and safe treatment strategies for both brain tumors and other resistant cancer types in the future. Future studies are recommended to evaluate the selectivity of SiPc (4) and SubPc (5) using non-malignant control cells and additional glioblastoma cell lines. Further analyses of cellular uptake, intracellular retention, subcellular localization, ROS generation, light-induced cytotoxicity, and optimized irradiation parameters would provide important insight into their biological and photodynamic potential. In addition, target-specific validation studies, including FAK phosphorylation, TOP2A activity, and DNA damage-related assays, may help clarify the molecular basis of the observed cellular responses.

CRediT authorship contribution statement

Şuranur Ayvaz: Writing – original draft, Methodology, Investigation, Data curation. **Nevzat Batan:** Writing – review & editing, Supervision, Resources, Methodology, Investigation, Conceptualization. **Cihan İnan:** Writing – review & editing, Validation, Supervision, Resources, Methodology, Investigation, Conceptualization. **Halil İbrahim Güler:** Writing – original draft, Methodology, Investigation, Data curation. **İsmail Değirmencioğlu:** Writing – review & editing, Writing – original draft, Supervision, Resources, Methodology, Investigation, Formal analysis, Data curation, Conceptualization.

Declaration of competing interest

The authors declare that they have no known competing financial interests or personal relationships that could have appeared to influence the work reported in this paper.

Appendix A. Supplementary data

Supplementary data to this article can be found online at https://doi.org/10.1016/j.jinorgbio.2026.113369.

References

[1] D. Hausmann, D.C. Hoffmann, V. Venkataramani, E. Jung, S. Horschitz, S. K. Tetzlaff, A. Jabali, L. Hai, T. Kessler, D.D. Azoŕin, S. Weil, A. Kourtesakis, P. Sievers, A. Habel, M.O. Breckwoldt, M.A. Karreman, M. Ratliff, J.M. Messmer, Y. Yang, E. Reyhan, S. Wendler, C. Löb, C. Mayer, K. Figarella, M. Osswald, G. Solecki, F. Sahm, O. Garaschuk, T. Kuner, P. Koch, M. Schlesner, W. Wick, F. Winkler, Autonomous rhythmic activity in glioma networks drives brain tumour growth, Nature 613 (2023) 179–186, https://doi.org/10.1038/s41586-022-05520-4.

[2] J. Chen, T. Fan, Z. Xie, Q. Zeng, P. Xue, T. Zheng, Y. Chen, X. Luo, H. Zhang, Advances in nanomaterials for photodynamic therapy applications: status and challenges, Biomaterials 237 (2020) 119827, https://doi.org/10.1016/j.biomaterials.2020.119827.

[3] W. Hua, W. Zhang, H. Brown, J. Wu, X. Fang, M. Shahi, R. Chen, H. Zhang, B. Jiao, N. Wang, H. Xu, M. Fu, X. Wang, J. Zhang, X. Zhang, Q. Wang, W. Zhu, D. Ye, D. M. Garcia, K. Chaichana, R.G. Cooks, Z. Ouyang, Y. Mao, A. Quinones-Hinojosa, Rapid detection of IDH mutations in gliomas by intraoperative mass spectrometry, Proc Natl Acad Sci 121 (2024) e2318843121, https://doi.org/10.1073/pnas.2318843121.

[4] J. Tan, X. Duan, F. Zhang, X. Ban, J. Mao, M. Cao, S. Han, X. Shuai, J. Shen, Theranostic nanomedicine for synergistic Chemodynamic therapy and chemotherapy of Orthotopic glioma, Adv Sci 7 (2020) 2003036, https://doi.org/10.1002/advs.202003036.

[5] M. Weller, M. van den Bent, M. Preusser, E. Le Rhun, J.C. Tonn, G. Minniti, M. Bendszus, C. Balana, O. Chinot, L. Dirven, P. French, M.E. Hegi, A.S. Jakola, M. Platten, P. Roth, R. Rudà, S. Short, M. Smits, M.J.B. Taphoorn, A. von Deimling, M. Westphal, R. Soffietti, G. Reifenberger, W. Wick, EANO guidelines on the diagnosis and treatment of diffuse gliomas of adulthood, Nat Rev Clin Oncol 18 (2021) 170–186, https://doi.org/10.1038/s41571-020-00447-z.

[6] Y. Jia, Y. Wu, F. Zhang, Y. Sun, Y. Liu, Overcoming the blood–brain barrier challenge: nanotechnology-enhanced photodynamic therapy for glioblastoma treatment, Chem Commun 61 (2025) 12431–12448, https://doi.org/10.1039/D5CC03192C.

[7] A. Aborode, R. Adesola, G. Scott, V. Adepoju, O. Akan, A. Ogunyemi, A. Adetunji, F. Arogundade, D. Somuah, A.O. Emmanuel, B. Ameh, I. Oluwaseun, A. Osu, V. Jonathan, C. Amadi, M. Oladayo, A. Matthew, I. Onifade, S. Fakorede, A. Bakre, Role of blood-brain barrier in bacterial translocation, Neuroscience 580 (2025) 99–114, https://doi.org/10.1016/j.neuroscience.2025.06.037.

[8] M.A. Dobrovolskaia, S.E. McNeil, Immunological properties of engineered nanomaterials, Nat Nanotechnol 2 (2007) 469–478, https://doi.org/10.1038/nnano.2007.223.

[9] M. Elsabahy, G.S. Heo, S.-M. Lim, G. Sun, K.L. Wooley, Polymeric nanostructures for imaging and therapy, Chem Rev 115 (2015) 10967–11011, https://doi.org/10.1021/acs.chemrev.5b00135.

[10] H. Baş, M.T. Muhammed, S. Akkoc, Z. Biyiklioglu, Synthesis, characterization and *in silico* evaluation of non-aggregating, water-soluble zinc(II) Phthalocyanines bearing pyridylpropoxy substituents as potential inhibitors of protein C, PAF acetylhydrolase, and ALDH enzymes, Inorg Chem Commun 183 (2026) 115872, https://doi.org/10.1016/j.inoche.2025.115872.

[11] H. Dummin, Th. Cernay, H.W. Zimmermann, Selective photosensitization of mitochondria in HeLa cells by cationic Zn(II)phthalocyanines with lipophilic side-chains, J Photochem Photobiol B 37 (1997) 219–229, https://doi.org/10.1016/S1011-1344(96)07416-7.

[12] T. Keleş, Z. Biyiklioglu, G. Seyhan, E. Öz, R. Reis, B. Barut, Highly water soluble metallophthalocyanines and investigation of their AChE/BuChE enzyme inhibition and cytotoxic activity against human neuroblastoma (SH-SY5Y) cell, Inorg Chem Commun 178 (2025) 114508, https://doi.org/10.1016/j.inoche.2025.114508.
[13] N. Malatesti, I. Munitic, I. Jurak, Porphyrin-based cationic amphiphilic photosensitisers as potential anticancer, antimicrobial and immunosuppressive agents, Biophys Rev 9 (2017) 149–168, https://doi.org/10.1007/s12551-017-0257-7.
[14] F. Çelik, Y. Ünver, F. OzTuncay, U. Cakmak, Y. Kolcuoglu, K.K. Uzun, H. Ozturk, N. Yorulmaz, İ. Değirmencioğlu, Synthesis and characterization of newly phthalocyanine molecules: their enzyme inhibition and antioxidant properties, in silico and in vitro, J Organomet Chem 1016 (2024) 123237, https://doi.org/10.1016/j.jorganchem.2024.123237.
[15] J. Guo, M. Sun, X. Meng, H. Zhu, C. Ma, S. Hu, J. Shen, Q. Wang, J. Gao, Impact of peripheral groups on novel asymmetric phthalocyanine-based hole-transporting materials for perovskite solar cells, Dyes Pigments 177 (2020) 108301, https://doi.org/10.1016/j.dyepig.2020.108301.
[16] İ. Tağman, M. Özçeşmeci, S. Gümrükçü, İ. Sorar, Spectroscopic, electrochemical and optical properties of non-peripherally (2,2-dimethyl-1,3-dioxolan-4-yl) methoxy groups substituted metal-free and metallophthalocyanines, J Mol Struct 1245 (2021) 131045, https://doi.org/10.1016/j.molstruc.2021.131045.
[17] E. Yabaş, M. Sülü, F. Dumludağ, B. Salih, Ö. Bekaroğlu, Imidazole octasubstituted novel mono and double-decker phthalocyanines: synthesis, characterization, electrical and gas sensing properties, Polyhedron 153 (2018) 51–63, https://doi.org/10.1016/j.poly.2018.06.044.
[18] B. Aldhubiab, R.M. Almuqbil, Polymeric nanoparticle-mediated photodynamic therapy: a synergistic approach for glioblastoma treatment, Pharmaceuticals 18 (2025), https://doi.org/10.3390/ph18071057.
[19] A. Nalçaoğlu, C. Sarı, İ. Değirmencioğlu, F.C. Eyüpoğlu, Novel piperazine-substituted silicon phthalocyanines exert anti-cancer effects against breast cancer cells, Photodiagn Photodyn Ther 37 (2022) 102734, https://doi.org/10.1016/j.pdpdt.2022.102734.
[20] C. Sarı, A. Nalçaoğlu, İ. Değirmencioğlu, F. Celep Eyüpoğlu, Tumor-selective new piperazine-fragmented silicon phthalocyanines initiate cell death in breast cancer cell lines, J Photochem Photobiol B 216 (2021) 112143, https://doi.org/10.1016/j.jphotobiol.2021.112143.
[21] M.A.A. Abdelhamid, S.P. Pack, Biomimetic and bioinspired silicifications: recent advances for biomaterial design and applications, Acta Biomater 120 (2021) 38–56, https://doi.org/10.1016/j.actbio.2020.05.017.
[22] W. Han, A. Chilkoti, G.P. López, Self-assembled hybrid elastin-like polypeptide/silica nanoparticles enable triggered drug release, Nanoscale 9 (2017) 6178–6186, https://doi.org/10.1039/C7NR00172J.
[23] C.R. Steven, G.A. Busby, C. Mather, B. Tariq, M.L. Briuglia, D.A. Lamprou, A. J. Urquhart, M.H. Grant, S.V. Patwardhan, Bioinspired silica as drug delivery systems and their biocompatibility, J Mater Chem B 2 (2014) 5028–5042, https://doi.org/10.1039/C4TB00510D.
[24] G. Yang, Y. Liu, H. Wang, R. Wilson, Y. Hui, L. Yu, D. Wibowo, C. Zhang, A. K. Whittaker, A.P.J. Middelberg, C.-X. Zhao, Bioinspired Core-Shell nanoparticles for hydrophobic drug delivery, Angew Chem 58 (2019) 14357–14364, https://doi.org/10.1002/anie.201908357.
[25] C. Cardenas Aguirre, The state of prostate Cancer around the world - advances in prostate, Cancer 6 (2023) 1–4, https://doi.org/10.4172/cocr.6(6).294.
[26] C. Cardenas Aguirre, A. Rosero, Comprehensive insights into human papillomavirus (HPV) and cervical cancer: progress, Therap Approach Prospects 2023 (6) (2023), https://doi.org/10.4172/cocr.6(6).298.
[27] C. Cardenas Aguirre, S. Abrishami, Colorectal Carcinoma: Review and Novelties 2023, 2023, p. 6, https://doi.org/10.4172/cocr.6(6).296.
[28] C. Cardenas Aguirre, Sarcomas: a comprehensive review of classification, diagnosis, Treat Psychosoc Aspects 6 (2023), https://doi.org/10.4172/cocr.6(6).295.
[29] Ü. Demirbaş, M. Pişkin, M. Durmuş, H. Kantekin, Metal or metal-free phthalocyanines containing morpholine substituents: synthesis, spectroscopic and photophysicochemical properties, J Coord Chem 75 (2022) 1243–1255, https://doi.org/10.1080/00958972.2022.2102906.
[30] Q. Guo, L. Chen, S. Pan, D. Ma, X. Liu, X. Chen, G. Xu, H. Yang, Y. Peng, Morpholinyl Dendrimer Phthalocyanine: Synthesis, Photophysical Properties and Photoinduced Intramolecular electron Transfer, 2018, https://doi.org/10.1039/C8DT02275E.
[31] M. Serhatli, S. Isik, A. Kalkan, M. Özçeşmeci, E. Hamuryudan, Ö. Can, Morpholinoethoxy-substituted cationic metal-free and metallo phthalocyanines: in vitro photodynamic therapy activities, PDT-induced ROS level measurements, and cellular death mechanism, ACS Bio Med Chem Au 5 (2025) 766–777, https://doi.org/10.1021/acsbiomedchemau.5c00137.
[32] S. Ayvaz, Z.B. Bolat, All-trans retinoic acid enhances anti-proliferative effect of dual PI3K and mTOR inhibitor NVP-BEZ235 in triple negative breast cancer, Naunyn. Schmiedebergs, Arch Pharmacol 398 (2025) 10855–10865, https://doi.org/10.1007/s00210-025-03981-8.
[33] G. Selimoglu, S. Ayvaz, Z.B. Bolat, BH3 mimetic and dual PI3K/mTOR inhibitor attenuates gemcitabine resistance in triple-negative breast cancer, Med Oncol 43 (2025) 10, https://doi.org/10.1007/s12032-025-03143-z.
[34] Y. Pommier, E. Leo, H. Zhang, C. Marchand, DNA topoisomerases and their poisoning by anticancer and antibacterial drugs, Chem Biol 17 (2010) 421–433, https://doi.org/10.1016/j.chembiol.2010.04.012.
[35] F.J. Sulzmaier, C. Jean, D.D. Schlaepfer, FAK in cancer: mechanistic findings and clinical applications, Nat Rev Cancer 14 (2014) 598–610, https://doi.org/10.1038/nrc3792.
[36] J. Zhou, Q. Yi, L. Tang, The roles of nuclear focal adhesion kinase (FAK) on Cancer: a focused review, J Exp Clin Cancer Res CR 38 (2019) 250, https://doi.org/10.1186/s13046-019-1265-1.
[37] T. Zhou, Y. Niu, Y. Li, Advances in research on malignant tumors and targeted agents for TOP2A (review), Mol Med Rep 31 (2025) 1–20, https://doi.org/10.3892/mmr.2024.13415.
[38] E.F. Pettersen, T.D. Goddard, C.C. Huang, E.C. Meng, G.S. Couch, T.I. Croll, J. H. Morris, T.E. Ferrin, UCSF ChimeraX, Structure visualization for researchers, educators, and developers, Protein Sci Publ Protein Soc 30 (2021) 70–82, https://doi.org/10.1002/pro.3943.
[39] M.D. Hanwell, D.E. Curtis, D.C. Lonie, T. Vandermeersch, E. Zurek, G.R. Hutchison, Avogadro: an advanced semantic chemical editor, visualization, and analysis platform, J Chemother 4 (2012) 17, https://doi.org/10.1186/1758-2946-4-17.
[40] G.M. Morris, R. Huey, W. Lindstrom, M.F. Sanner, R.K. Belew, D.S. Goodsell, A. J. Olson, AutoDock4 and AutoDockTools4: automated docking with selective receptor flexibility, J Comput Chem 30 (2009) 2785–2791, https://doi.org/10.1002/jcc.21256.
[41] N.S. Pagadala, K. Syed, J. Tuszynski, Software for molecular docking: a review, Biophys Rev 9 (2017) 91–102, https://doi.org/10.1007/s12551-016-0247-1.
[42] B. Barut, Z. Biyiklioglu, C.Ö. Yalçın, M. Abudayyak, Non-aggregated axially disubstituted silicon phthalocyanines: synthesis, DNA cleavage and in vitro cytotoxic/phototoxic anticancer activities against SH-SY5Y cell line, Dyes Pigments 172 (2020) 107794, https://doi.org/10.1016/j.dyepig.2019.107794.
[43] D. Ma, X. Chen, Y. Wang, Q. Guo, Q. Ye, R. Guo, S. Xiao, Q. Ye, Y. Huang, Y. Peng, Benzyl ester dendrimer silicon phthalocyanine based polymeric nanoparticle for in vitro photodynamic therapy of glioma, JOL 207 (2019) 597–601, https://doi.org/10.1016/j.jlumin.2018.12.012.
[44] Z. Bıyıklıoğlu, İ. Öztürk, T. Arslan, A. Tunçel, K. Ocakoglu, M. Hosgor Limoncu, F. Lambrecht, Synthesis and antimicrobial photodynamic activities of axially {4-[(1E)-3-oxo-3-(2-thienyl)prop-1-en-1-yl]phenoxy} groups substituted silicon phthalocyanine, subphthalocyanine on Gram-positive and Gram-negative bacteria, Dyes Pigments 166 (2019), https://doi.org/10.1016/j.dyepig.2019.03.010.
[45] H.T. Önal, A. Yuzer, M. Ince, F. Ayaz, Photo induced anti-inflammatory activities of a Thiophene substituted subphthalocyanine derivative, Photodiagn Photodyn Ther 30 (2020) 101701, https://doi.org/10.1016/j.pdpdt.2020.101701.
[46] A.R. Dwivedi, V. Kumar, V. Prashar, A. Verma, N. Kumar, J. Parkash, V. Kumar, Morpholine substituted quinazoline derivatives as anticancer agents against MCF-7, A549 and SHSY-5Y cancer cell lines and mechanistic studies, RSC Med Chem 13 (n.d.) 599–609. doi:https://doi.org/10.1039/d2md00023g.
[47] M. Gallardo-Villagrán, L. Paulus, D.Y. Leger, B. Therrien, B. Liagre, Dimethyl sulfoxide: a bio-friendly or bio-Hazard chemical? The effect of DMSO in human fibroblast-like synoviocytes, Molecules 27 (2022), https://doi.org/10.3390/molecules27144472.
[48] A.A.A. Awadh, E.E. Hassan, O.M. Shoaib, O.A.E. Elnoubi, S.A. Mustafa, Y. M. Althayrayan, M.A. Althayrayan, M.M. Alshahrani, Anethole inhibits human U87 glioma cell proliferation by inducing apoptosis via the PI3K/AKT pathway, PLoS One 20 (2025) e0336975, https://doi.org/10.1371/journal.pone.0336975.
[49] Y.-P. Fan, P. Liu, W.-K. Xue, W.-J. Zhao, H.-C. Pan, Trimebutine promotes glioma cell apoptosis as a potential anti-tumor agent, Front Pharmacol 9 (2018) 664, https://doi.org/10.3389/fphar.2018.00664.
[50] Adel M. Kamal, A.A. El-Dean, R. Geies, F.K. Hassanien, E.E.A. El-Naeem Abdel-Wadood, Novel synthesis, reactions, and biological study of new morpholino-Thieno[2,3-c][2,7]Naphthyridines as anti-cancer and anti-microbial agents, Russ J Bioorgan Chem 48 (2022) 821–834, https://doi.org/10.1134/S1068162022040021.
[51] Q.R. Liu, J.M. Liu, Y. Chen, X.Q. Xie, X.X. Xiong, X.Y. Qiu, F. Pan, D. Liu, S.B. Yu, X. Q. Chen, Piperlongumine inhibits migration of glioblastoma cells via activation of ROS-dependent p38 and JNK signaling pathways, Oxidative Med Cell Longev 2014 (2014) 653732, https://doi.org/10.1155/2014/653732.
[52] W. Tang, M. Zhao, C. Gao, L. Fu, S. Wang, D. Qin, Y. Tian, X. Wang, Unexpected synthesis and anticancer activity evaluation of a smart lysosome-targeted photosensitizer based on BODIPY, Dyes Pigments 248 (2026) 113552, https://doi.org/10.1016/j.dyepig.2026.113552.
[53] E. Lenci, L. Calugi, A. Trabocchi, Occurrence of Morpholine in central nervous system drug discovery, ACS Chem Neurosci 12 (2021) 378–390, https://doi.org/10.1021/acschemneuro.0c00729.